P 1.2

McGILL ALGORITHM FOR PRECIPITATION NOWCASTING BY LAGRANGIAN EXTRAPOLATION (MAPLE) APPLIED TO THE SOUTH KOREAN RADAR NETWORK. PART 1: SENSITIVITY STUDIES OF THE VARIATIONAL ECHO TRACKING (VET) TECHNIQUE

Hee Choon Lee,
Korea Meteorological Administration, Seoul, South Korea

A. Bellon*, I. Zawadzki and A. Kilambi,
J. S. Marshall Radar Observatory, McGill University, Montreal, Canada

1. INTRODUCTION

The McGill Algorithm for Precipitation nowcasting by Lagrangian Extrapolation (MAPLE) has being applied in real-time with data from the South Korean radar network. This procedure first determines a radar echo velocity field using a Variational Echo Tracking (VET) technique and then generates a nowcast by Lagrangian advection of the current map by assuming stationarity of the derived vector field throughout the forecast period. The VET technique as first presented by Laroche and Zawadzki (1995) was actually devised for wind retrievals over a very small region of 20 km by 20 km using both reflectivity and Doppler data sets. It has then been adapted to reflectivity-only maps over domains larger by about two orders of magnitude as is the case with the United States radar network. A basic description of MAPLE is provided by Germann and Zawadzki (2002), the extension to probabilistic forecasts has then been formulated by Germann and Zawadzki (2004), the implementation of a filtered forecast that removes the perishable scales has been carried out by Seed (2003) and by Turner et al. (2004) while the limits of predictability have been examined with a much larger data set by Germann et al. (2006).

In this Part 1 of our two-part research effort we first examine the influence of the various user-selectable VET parameters on the skill of the resulting 20-min to 4-h forecasts using four months of archived data from South Korea (July and Nov ’06, Feb and May ‘07) provided to us before the real-time experiment. We briefly describe in section 2 the Korean radar data and then, in section 3, the VET module and its main input parameters. In section 4 we outline the semi-Lagrangian advection scheme and illustrate an example of a MAPLE forecast. Section 5 analyzes the verification results obtained with the ‘default’ VET input parameters as well as with other plausible combinations. The results of the real-time experiment conducted in the summer of 2008 in South Korea is presented in the accompanying Part 2 paper.

Corresponding author address: Aldo Bellon, J. S. Marshall Radar Observatory, P. O. Box 198, Macdonald Campus, Ste-Anne-de-Bellevue, QC, Canada.
H9X 3V9 E-mail: aldo.bellon@mcgill.ca

2. ADAPTATION OF THE KOREAN COMPOSITE DATA INTO MAPLE

The Korean composite radar network is composed of data from a maximum of 11 radars with an update cycle of 10 minutes. The composite map used as VET input is based on the so-called CMAX map that picks up the strongest reflectivity among all the available elevation angles. The individual CMAX maps from each radar are then combined into the ‘composite’ radar map of the Korean network by using the maximum algorithm, that is, the strongest reflectivity is shown over overlapping coverage. The chosen method of map projection is a Lambert Conic Conformal true at the two standard parallels of 30º N and of 60º N latitude, thus assuring a minimal amount of distortion with respect to the true distances along the surface of the earth. The resulting composite map consists of a (512 x 512) array at 2-km resolution, covering the entire Korean Peninsula and neighboring territories. Examples are provided in Fig. 1.

3. VARIATIONAL ECHO TRACKING (VET) TECHNIQUE

3.1 Basic description of VET

An adaptation of the variational echo tracking (VET) technique described by Laroche and Zawadzki (1995) is used to derive the velocity field of radar reflectivity echoes. The entire composite map is divided into sub-domains of a selectable size and a velocity vector $\boldsymbol{V}_{m,n}$ can be computed for each sub-area *(m,n)* by minimizing the difference, or cost function, in the reflectivity between two composite maps $Z(x,y,t_o)$ and $Z(x,y,t_o\text{-}\Delta t)$ separated by a certain time interval Δt. To construct the whole field $\mathbf{V}=\boldsymbol{V}_{mn}$ each $\boldsymbol{V}_{m,n}$ vector can be retrieved by an individual minimization inside each sub-area, or, as is specific to the variational method, all vectors are retrieved simultaneously by performing a global minimization over the entire composite map. A smoothness constraint is also applied in order to reduce any drastic differences between the vectors at neighboring sub-areas. The cost function *F* to be minimized thus depends totally on the vector field **V** and may be expressed in terms of these two constraints as follows:

$$F(V) = F_Z + F_V \tag{1}$$

The conservation of reflectivity constraint F_Z is explicitly defined as the sum of squares of the residuals at all (x,y) points, (in practice, at all grid areas (i, j) of the domain), as one map is displaced over the other according to the vector field $\mathbf{V}_{x,y}$**=(u,v),** where **u** and **v** are the x- and y-components of **V** interpolated at every (x,y) from the $V_{m,n}$ values at neighboring sub-areas.

$$F_Z = w_z \Sigma_x \Sigma_y \left\{ Z(x,y,t_o) - Z(x-u\Delta t, y-v\Delta t, t_o-\Delta t) \right\}^2 dxdy$$

w_z is a weight given to this conservation of reflectivity constraint. It is generally related to data quality, but in most applications, is made to be a constant throughout the domain of integration. The domain of integration should be smaller than the actual extent of the composite map in order to ensure that the offset displacement (x-$u\Delta t$, y-$v\Delta t$) remains within the composite map. The second term of Eq. (1) is a smoothness penalty function that limits the variability in space of the V_{mn} vectors. It is defined as

$$F_V = w_v \Sigma\Sigma \left\{ (d^2u/dx^2)^2 + (d^2u/dy^2)^2 + 2(d^2u/dxdy)^2 + (d^2v/dx^2)^2 + (d^2v/dy^2)^2 + 2(d^2v/dxdy)^2 \right\} dxdy$$

where the integration is only over the (m x n) sub-areas for which a velocity V_{mn} is estimated and w_v is the weight given to this smoothness constraint. For the sake of efficiency, the gradient of the cost function is derived as a function of the velocity estimates in order to direct the updated guesses along the proper direction leading to the true minimum of the overall cost function. Several iteration or guesses, (of the order of 100), are attempted in order to locate this minimum. In VET, we use the conjugate-gradient algorithm described by Navon and Legler (1987) to determine the optimum search direction and the step length. In order to reduce the probability of converging towards a secondary minimum, we have developed a scaling-guess procedure in which the field is iteratively retrieved with increasing grid resolution. For example, a coarse resolution $V_{5,5}$ field first derived over (5x5) sub-areas is used as an initial guess for the final $V_{25,25}$ field derived over (25 x 25) sub-areas. We point out that the retrieved vector field V_{mn} is most reliable in the regions of precipitation echoes, whereas far away from any precipitation area the vectors must be interpreted with care, being either extrapolated values or the result of tracking a few isolated echoes.

3.2 Description of the user-selectable input parameters for the VET module.

There is a non-negligible number of user-selectable parameters required as input to the VET module that can affect its performance. However, we had anticipated that *a*) there is no single combination that is optimum for all weather events and *b*) that the optimum combination will be only slightly better than one that has been reasonably well devised. We thus simply provide a list and a brief description for only those that are most relevant to the research presented here. The 'default' choice for each parameter is in parenthesis.

1- Number of maps	(3)
2- Time difference between each map	(20 min)
3- Amount of smoothing	(3x3) pixels)
4- Reflectivity threshold	(15 dBZ)
5- Number of scaling guesses	(2)
6- Vector density of each scaling guess	(5x5) and (25x25)
7- Relative weights for w_z and w_v	(0.5 and 1000.0)
8- Temporal smoothing	(yes)

- <u>*Number of maps and their time difference*</u>: A minimum of two maps separated by any time difference is required in order to estimate the relative motion of precipitation echoes. However a minimization procedure performed over both the [$Z(t_o)$, $Z(t_o$-$\Delta t)$] pair as well as over the [$Z(t_o$-$\Delta t)$], $Z(t_o$-$2\Delta t)$] pair would be more robust than a similar procedure over simply the entire [$Z(t_o)$, $Z(t_o$-$2\Delta t)$] combination because the former better takes into account the temporal evolution of the echo velocities and reduces the possibility of matching unrelated echoes. The choice of Δt is dictated by the temporal resolution of the data set. In our case, this time interval is forcibly a multiple of the radar scanning cycle of 10 minutes. A small Δt ensures that the precipitation pattern has not changed to such a large extent that no recognizable features remain. In fact, a large Δt may cause the pattern recognition technique to latch on to unrelated echoes and thus yield spurious velocities vectors. On the other hand, considering that the ultimate goal is to use the velocity field deduced from VET in order to generate precipitation forecasts of up to at least three hours, a short 20-minute interval is not suitable for such a goal because it may incorporate short-lived accelerations or decelerations that are not expected to persist over the forecasting period. It thus seems evident that if we decide on using 3 maps, then the obvious choice would be Δt = 20 minutes so that the ratio of the historical to the forecasting interval, that is, 40/180 is not too small for a 3-hr forecast.

- <u>*Amount of smoothing*</u>: Instantaneous radar reflectivity maps are inherently noisy at smaller spatial scales of 1 or 2 km and this characteristic may have a negative impact on the ability of any pattern recognition technique to identify features that are evolving in time. Thus it is preferable to remove any random noise by smoothing the composite maps. The amount of smoothing is simply achieved by averaging the 2-km resolution data over a (3x3) or (5x5) neighborhood.

- *Reflectivity Threshold*: A radar map may have echoes ranging from -20 to 60 dBZ. For the goal of computing velocities for forecasting purposes it is not desirable to track echoes with very weak reflectivity because these are likely shorter-lived compared with stronger echoes. Weak reflectivities may also be associated with snow observed at higher altitudes at very far ranges, and thus their apparent motion may not be related to the actual motion of rain echoes below it. For summer precipitation a threshold of 15 to 20 dBZ appears to be adequate.

- *Number and vector density of the scaling guesses*: In the absence of any other information, Laroche and Zawadzki (1994) have developed a scaling-guess procedure in which the field is iteratively retrieved with increasing grid resolution. A three-step scaling procedure is well illustrated in Fig. 7 of Germann and Zawadzki (2002). Since then we have found that the 'single-vector' scaling step can be skipped such that the coarser scale involves at least (4x4) vectors followed by a 2nd and final scaling that yields the desired density of the vector field. The latter should be chosen small enough to allow for large- and medium-scale rotation, deformation and differential motion between precipitation areas in different regions. But it should be large enough to avoid tracking the perishable convective scales, particularly if, as already mentioned, it is to be used for forecasts of the order of three hours. The number of vectors selected for any scale step must be exactly divisible into the size of the array over which the minimization is performed. In order to avoid boundary problems, this size has been chosen to be (400x400) for the Korean composites. A set of (25x25) or (50x50) vectors is thus possible.

- *Relative weights for w_z and w_v*: Both w_z and w_v are user-selectable at every scaling resolution but since the total number of (i, j) pixels is typically three orders of magnitude larger than the (m x n) sub-areas, then the ratio w_v/w_z should follow a similar correspondence, as for example, w_z=0.5 and of w_v= 1000.

- *Temporal smoothing*: Even after the application of the smoothing constraint in the spatial domain that is inherently part of the VET algorithm, the resultant velocity field may still incorporate some undesirable fluctuations which are noticeable when the images are animated in time. These temporal differences are a reflection of some minor instability about a mean motion, or the result of a deviation from the true motion due to some data artifacts and they could lead to slightly worse forecasts when extrapolated hours ahead. It has thus become a practice in nowcasting methodology to derive the final vector field $\boldsymbol{V_f}$ by weighing the current realization $\boldsymbol{V_c}$ with that of the previous cycle $\boldsymbol{V_p}$, that is, $\boldsymbol{V_f}=w_c\boldsymbol{V_c}+ w_p\boldsymbol{V_p}$. We have arbitrarily chosen the weights to be w_c=0.6 and w_p=0.4. Note that since $\boldsymbol{V_p}$ already incorporates a temporal smoothing, the vectors determined at the antecedent cycles also have a non-negligible but diminishing influence on $\boldsymbol{V_f}$.

4- DESCRIPTION OF THE SEMI-LAGRANGIAN ADVECTION SCHEME

After obtaining the velocity field of the precipitation pattern at the desired vector density according to the VET procedure, the actual forecasts are generated using a semi-Lagrangian advection scheme as proposed by Germann and Zawadzki (2002). The advantage of a field of velocity vectors is that, unlike with the single or constant vector, it allows for differential motion during the forecasting process and is thus capable of simulating rotation at the near synoptic scale of the composite radar maps.

From the velocity field available at the (m x n) sub-areas, where typically (m x n) = (25 x 25), a velocity vector in units of grid lengths per time step is first derived by bilinear interpolation at every grid area of the composite map. The actual forecast map is then generated using the so-called semi-Lagrangian scheme which divides the entire forecast period T into N steps of length Δt such that $N\Delta t = T$. The advection time step is somewhat arbitrary, but Δt = 1 minute is considered sufficiently small to simulate the actual motion without introducing quantization effects. After each time step, the velocity vector of the nearest grid area is taken in order to determine the length of the subsequent step. The final displacement vector is the vector sum of the N fractional vectors of the individual time steps. Stationarity of the velocity field is assumed, Germann et al. (2006). There remains the choice of an advection scheme that is either '*forward in time and downstream in space*' or '*backward in time and upstream in space*'. In order to avoid 'holes' in the resultant forecast map caused by a region of divergence, a forward scheme requires the redistribution or spreading of the advected value to neighboring grid points according to some subjective radius of influence. In order to avoid this problem, a backward scheme is preferred, that is, we move upstream from the grid area (i,j) for which a forecast is desired in order to determine the origin (i_o,j_o) of a parcel that would end up at (i,j). When (i,j) is in a divergent region, the forecast for its neighboring grid areas may have the same source at (i_o,j_o), that is, the same (i_o,j_o) pixel is assigned to more than one pixel in the neighborhood of (i,j), thus causing a stretching or increase in area of the forecast precipitation. Conversely, when (i,j) is in a convergent region, the result is a decrease in the forecast area of precipitation compared to that observed at the time of forecast. Both effects combine to distort the original configuration of the rainfall pattern. This departure from the conservation of mass, (rainfall flux or reflectivity), thus depends on the degree of convergence or divergence of the VET velocity field.

The number and frequency of forecasts are user-selectable, a typical specification being 12 forecasts spaced 20 minutes apart, from 20-min to a 4-h forecast. An example of a 2- and of a 4-h forecast

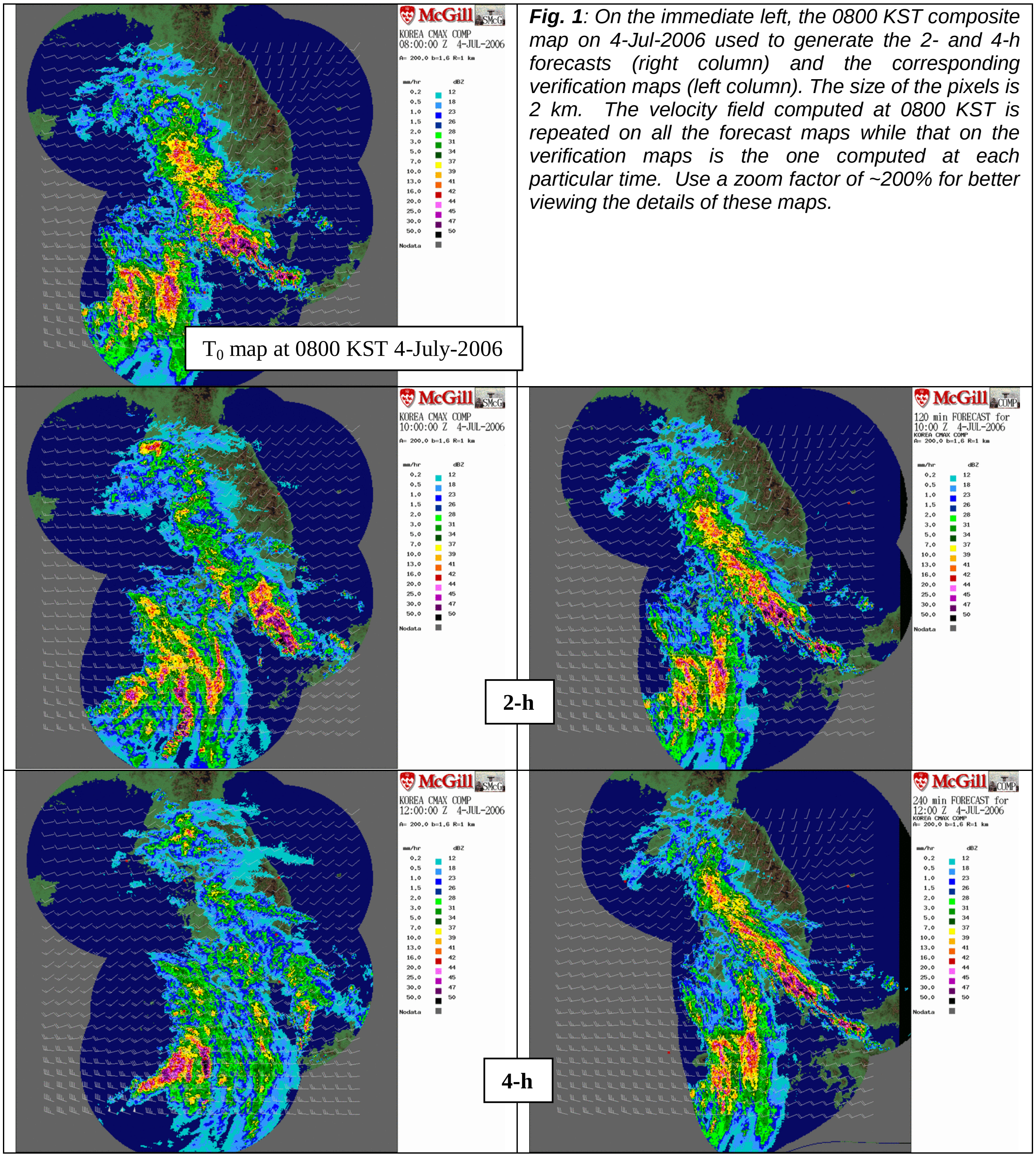

Fig. 1*: On the immediate left, the 0800 KST composite map on 4-Jul-2006 used to generate the 2- and 4-h forecasts (right column) and the corresponding verification maps (left column). The size of the pixels is 2 km. The velocity field computed at 0800 KST is repeated on all the forecast maps while that on the verification maps is the one computed at each particular time. Use a zoom factor of ~200% for better viewing the details of these maps.*

with the corresponding verification map is illustrated in Fig. 1. With faster velocities from the west in the southerly portion of the composite map coupled with slower motion from the south or southwest being deduced for the northern section, the distortion of the original image becomes more and more apparent as the length of the forecast increases. Note that at 0800 KST, the southwestern portion of the precipitation pattern is cut off by the maximum range of the radar. This artificial feature is of course advected forward together with the nodata region behind it. As a result, no comparisons can be made with the corresponding pixels of the verification map even though measurements are available. For this example, the forecasts reasonably match the verification maps since the faster speed in the south and the slower speeds in the north persisted throughout the forecast period. However, any new growth or dissipation of the precipitation pattern cannot be predicted using this "status quo" method. Some of the changes are real, like the area of heavy rain that developed in the south by 1200 KST, while others, like the weakening by 1200 KST of the high rainfall rates in the rainband just off the south coast of the Korean Peninsula may be due range effects. Calibration differences among the various radars can also cause an apparent reduction in forecast skill that should not be attributed to the forecast methodology. One way to partly circumvent this problem is to ignore the fine scale differences and to compare maps at a much coarser resolution, or in terms of thresholds as is the case with the Critical Success Index (CSI).

5- VERIFICATION

The forecast skill has been assessed by means of the usual parameters of probability of detection (POD), the false-alarm rate (FAR) and the critical success index (CSI). These scores describe the skill in predicting the occurrence of precipitation above a given threshold rate, which, as just stated, is quite suitable for our purpose. The forecast and verification map is treated as a binary image of 'event' or of 'no event' with respect to the selected threshold, excluding of course the 'nodata' region. Then, for each pixel, we define variables as follow: a = hits, b = misses, c = false alarms, d = both 'no event'. For the sake of brevity, we will present and discuss only the CSI scores. Its familiar formulation becomes

$$\mathrm{CSI} = a/(a+b+c)$$

Note that the significant changes in intensity between the predicted and actual precipitation pattern that occur far above or below the selected threshold do not affect the value of the above skill scores. Thus, in order to partly compensate for this inadequacy, skill scores for 7 rainfall rate thresholds of 0.1, 0.2, 0.5, 1, 2, 5 and 10 mm/hr have been derived. For information purposes, the per cent frequency distribution of these rates has been found to be 11.5, 23.1, 18.5, 17.4, 17.7, 7.8 and 4.0% respectively from the 4-month data set.

5.1 Verification results using the default VET input parameters

We have first verified the forecasts using the default VET input parameters as defined in section 3.2. The comparison is performed after applying a (3x3) smoother to both the forecast and verification maps, implying an effective resolution of 6 km. In order to avoid nearby ground clutter or strong bright band features as well as far range effects, pixels within 8 km from any radar, or beyond 200 km from all the radars are excluded. We have verified all forecasts for which the echo coverage on the smoothed verification map, defined as a rainfall rate in excess of 0.1 mm/h, exceeded 1000 pixels (4000 km^2). On account of the various precipitation episodes during the 4-month data set, the number of verifiable forecasts made every 20 minutes depends on the length of the forecast, (~3036, the equivalent of 42 days of continuous data for the 20-minute forecasts and decreasing to ~2635 for the 240-minute forecasts).

There are two options in presenting the final results: 1) In terms of an *overall* score obtained by first summing into the variables a, b and c all the binary comparisons of the entire test and then computing CSI and 2) in terms of the *average* score obtained by computing CSI for each individual forecast and then dividing by the number of forecasts. With this latter option, we have subjectively required that the denominator in the CSI definition exceed 100 pixels. The *overall* score is weighted by the radar coverage while all the individual forecasts contribute equally to the *average* score after having satisfied the 100 pixels requirement. We tend to prefer the *overall* score because it avoids the need for such a subjective requirement prior each comparison. Since the magnitude of the individual scores tends to increase with radar coverage, the overall scores are generally higher than the average scores as shown in Fig. 2.

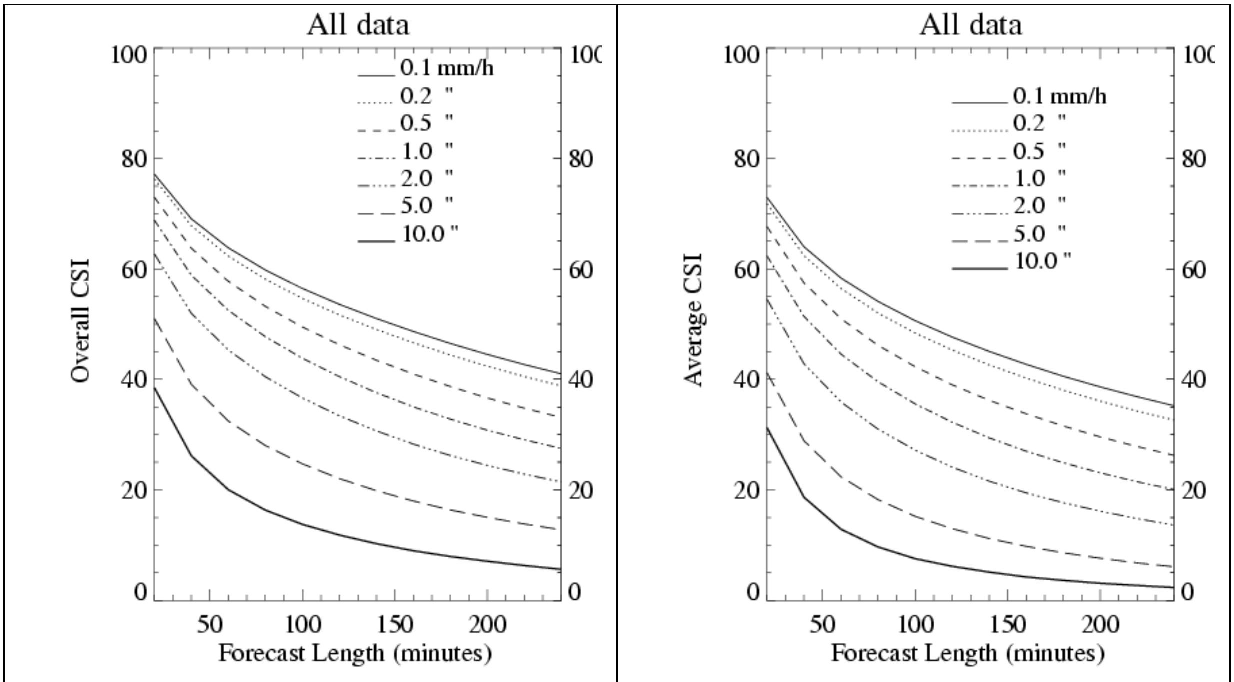

Fig. 2: *'Overall' and 'average' CSI scores as a function of forecast length and of the indicated rainfall rate thresholds obtained from the entire 4-month data set using the default VET inputs and after applying a (3x3) smoother to the observed and forecast maps at 2-km resolution*.

The decrease of the CSI with forecast length and with increasing rainfall rate is well illustrated. The steepest drop with the forecast length occurs before the first 100 minutes and then falls off in a linear fashion. The inability to accurately forecast higher rainfall rates (> 5 mm/h) is evidenced by overall (average) CSI scores of the order of 20% and less for forecasts longer than just two (one) hours. We prefer to use the CSI skill scores at the 0.5 mm/h rain rate level, (rather than the 'rain-no-rain' threshold of 0.1 mm/h) because of its greater hydrological relevance. We thus obtain overall CSI scores of 58, 46, 39 and of 30% for 1-, 2-, 3- and 4-h forecasts respectively. Comparison of these scores with those reported on our publications is not necessarily recommended because of their different geographical location and of their known dependence on the type of precipitation and resolution scale. The usefulness of these scores is not in their absolute magnitude but in assessing the relative skill of forecasts obtained with vectors derived with different VET inputs, or under different verification constraints.

The major source of error of the presented scores is mainly due to the inherent inability of any nowcasting procedure to forecast the position of an intensity cell with an accuracy equivalent to the 2-km resolution of the map, a direct consequence of the stochastic rearrangement of the structure of precipitation patterns that occurs even within relatively short periods of time, of the order of minutes. This observation supports our earlier argument regarding the stochastic nature of the precipitation patterns being a limiting factor in forecasting skill. This statement will

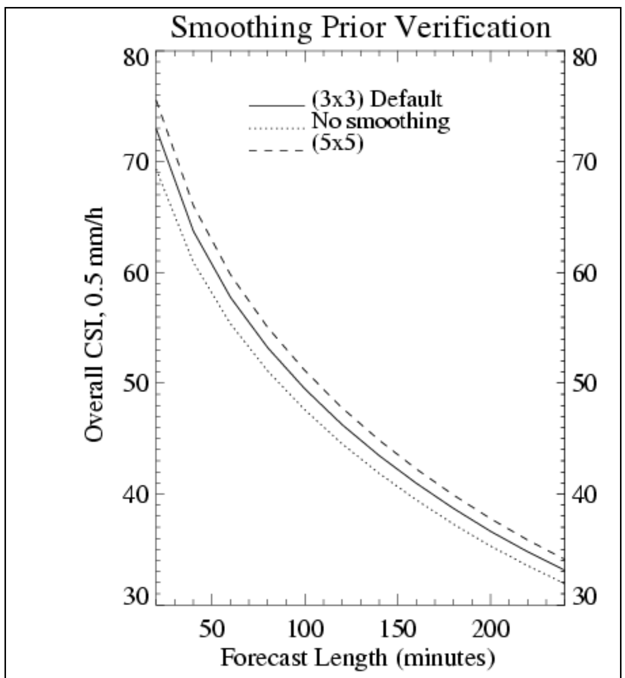

Fig. 3: *Variation of the overall CSI for 0.5 mm/h with the level of smoothing applied to the observed and forecast maps prior verification.*

remain true even if storm growth and decay were to be successfully taken into account.

The uncertainty in the detailed structure of precipitation patterns can of course be circumvented by additional smoothing prior the verification procedure, resulting in improved scores as shown in Fig. 3 where a (5x5) smoother has been attempted. Here, and in subsequent results, we have selected the score from the CSI parameter for a rain rate of 0.5 mm/h as representative of all the other scores obtained. Additional smoothing and removal of perishable information as described by Turner et al. (2004) and by Germann et al. (2006) becomes essential when precipitation nowcasts are to be assimilated into other algorithms such as hydrological modeling.

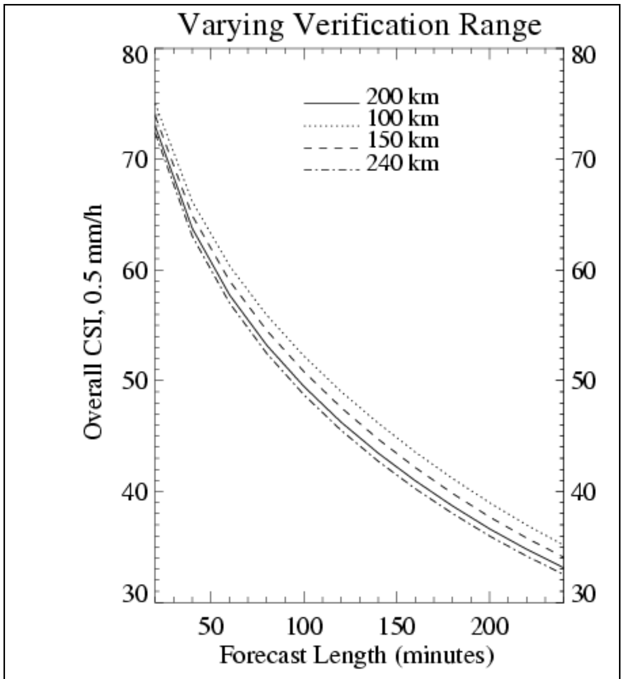

Fig. 4: *Variation of the overall CSI for 0.5 mm/h with the maximum range of verification.*

The discrepancy between the forecast and observed maps is also due to the quality of the radar data. This quality is known to be reduced as the radar range increases, thus affecting the verification scores as illustrated in Fig 4. CSI scores are seen to be appreciably increased when comparisons are done only over pixels that are relatively close (<100 km) to at least one radar. Other factors like calibration differences among the various radars of the network are not taken into account by this analysis.

5.3 Verification results after varying the VET input parameters

We now examine how a modification of the various default VET input parameters affect the quality of the resultant forecasts. We begin with Fig. 5 showing how a different choice for the density of the final vector field, that is, a (5x5) and (50x50) rather

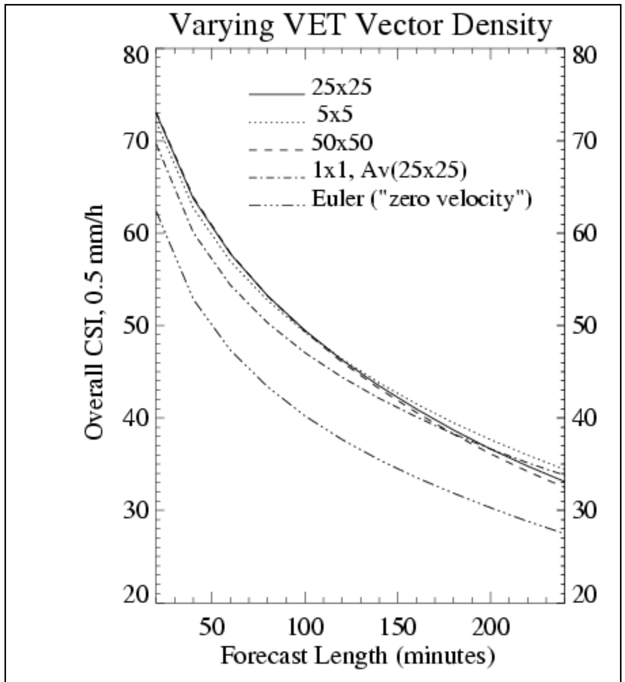

Fig. 5: *Variation of the overall CSI for 0.5 mm/h as a function of the VET vector density. The curve for a 'single' vector computed from the average of the (25x25) vector field as well as that obtained after assuming 'zero velocity' are also shown*.

than the default of (25x25), affects the CSI scores for rain rates of 0.5 mm/h. In addition we show two other curves: one obtained from a 'single' vector forecast and the other representing the Eulerian forecast, that is, the assumption of 'zero velocity' of the precipitation pattern, or, persistence in time and space. The 'single' vector has been computed from the vector sum of the default (25x25) field of vectors. We realize that the density of vectors only marginally affects the final outcome, with the sparse (5x5) field performing slightly better for forecasts longer than 2 hours and negligibly worse for shorter forecasts as may have been expected. The more detailed (50x50) field fails to even negligibly improve the short-term forecasts and is slightly worse that the default beyond 2 hours. These results are related to the expected persistence of the velocity fields which seem to behave in a manner equivalent to that for reflectivity fields. Therefore, just as in the case of the small perishable reflectivity scales, the detailed motion of a precipitation pattern is not expected to be long lasting while the coarser field has greater forecastability in the longer term. In fact, a close examination of the curves beyond 3 hours reveals that the single vector forecasts are actually better than those from the default (25x25) vector field, and only slightly inferior to those from the (5x5) field. In Fig. 5 the curve representing the results of an

Eulerian forecast obtained by assuming no velocity of the precipitation patterns is meant to be interpreted as the level of no skill. The difference of the Lagrangian curves from this Eulerian curve is interpreted as the skill provided by the Lagrangian advection scheme. The magnitude of the Eulerian score is related to the scale length (echo coverage) of the precipitation pattern to a greater extent than the Lagrangian forecasts. Hence this difference is not as large as may have been anticipated on account of the relatively extensive precipitation areas present over the Korean Peninsula during the period analyzed.

In Fig. 6, we explore the effects of varying three of the VET input parameters but as we can see, the three curves are virtually overlapping, and hence the results are essentially unchanged. The curve labeled “2 maps” has been derived using only two maps 20 minutes apart, rather than the default of 3 maps at T_0, T_0-20 minutes and T_0-40 minutes. The second curve giving the scores obtained without temporal smoothing likewise yield undistinguishable results. Negligibly improved scores seem to be obtained for shorter term forecasts with the third curve in which a (5x5), rather than the default (3x3) smoother, has been applied to the three composite radar maps prior their use by the VET algorithm.

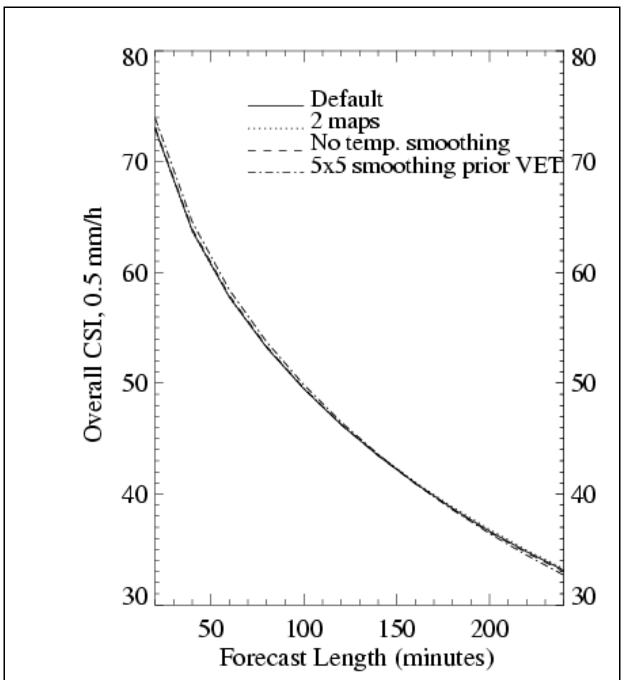

Fig. 6*: Variation of the overall CSI for 0.5 mm/h as a function of three different sets of inputs to VET. See the text for more details.*

We next examine the results obtained by varying the minimum reflectivity threshold from its default value of 15 dBZ. The VET procedure sets to ‘no echo’ all reflectivities below the selected threshold, which thus have no influence on the computation of the velocity field. The velocity field obtained with a higher threshold should thus be more appropriate for the motion of the stronger intensities. However, because of the requirement of at least 1000 pixels with a reflectivity above the selected threshold for the VET procedure to be attempted, the number of forecasts

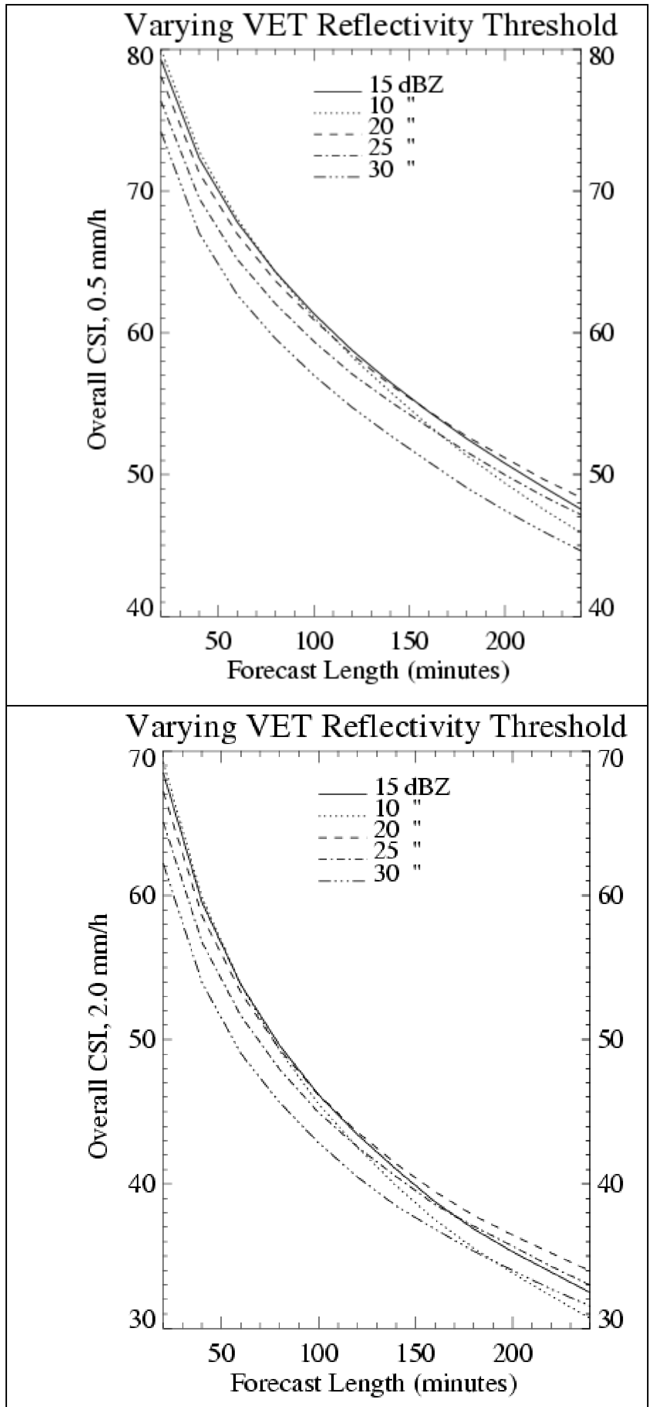

Fig. 7*: Variation of the overall CSI for 0.5 and 2.0 mm/h as a function of the VET reflectivity threshold for a selected subset of five events from the entire sample.*

made and then verified is a strong function of this threshold. Thus, when this test was applied to the entire 4-month sample, the result was strongly affected by sampling differences. It is thus necessary to only verify a sample for which the same number of forecasts is made. This has been achieved by selecting five events with strong and widespread precipitation patterns resulting into about 310 and 255 forecasts respectively for the 20-min and 4-h forecast length for all thresholds attempted. The verification curves for the 0.5 mm/h rate reveal that the default threshold of 15 dBZ is very close to being the optimum choice for the entire forecast period, with the 20 dBZ threshold being marginally better for forecasts beyond 3 hours. For the forecast of rainfall rates > 2.0 mm/h, the 20 dBZ threshold provides a measurable improvement after 2.5 hours. However, it may not be considered sufficiently large to justify a hybrid-procedure that use vector fields derived from different thresholds depending on the rain rates being forecasted. Note that the 10 dBZ threshold which is of equal skill as the default 15 dBZ threshold for shorter forecasts, is progressively less skillful for longer forecasts, particularly, as may be expected, for the higher rain rate of 2.0 mm/h. The nowcasting from velocity vectors obtained from cells 30 dBZ and higher are seen to be less reliable, yielding worse forecasts, regardless of forecast length and rain rate intensity.

The effects of varying the weights assigned to the constraint for the conservation of reflectivity and to the velocity smoothing constraint are examined in Fig. 8a and 8b respectively. We realize once again, that in spite of the fact that the weights have been altered drastically from their default values of w_z=0.5 and w_v=1000, differences in the outcome are barely noticeable. Note that the combination (w_z=0.1, w_v=1000) is equivalent to (w_z=0.5, w_v=5000), both providing a relatively higher weight to the smoothing constraint and (w_z=5.0, w_v=1000) is equivalent to (w_z=0.5, w_v=100), both favoring a higher weight for the conservation of reflectivity. The latter yields more spatially variable velocity fields and thus are seen to result into negligibly worse forecasts compared with the more smoothly varying fields obtained by giving a higher weight to the smoothing constraint.

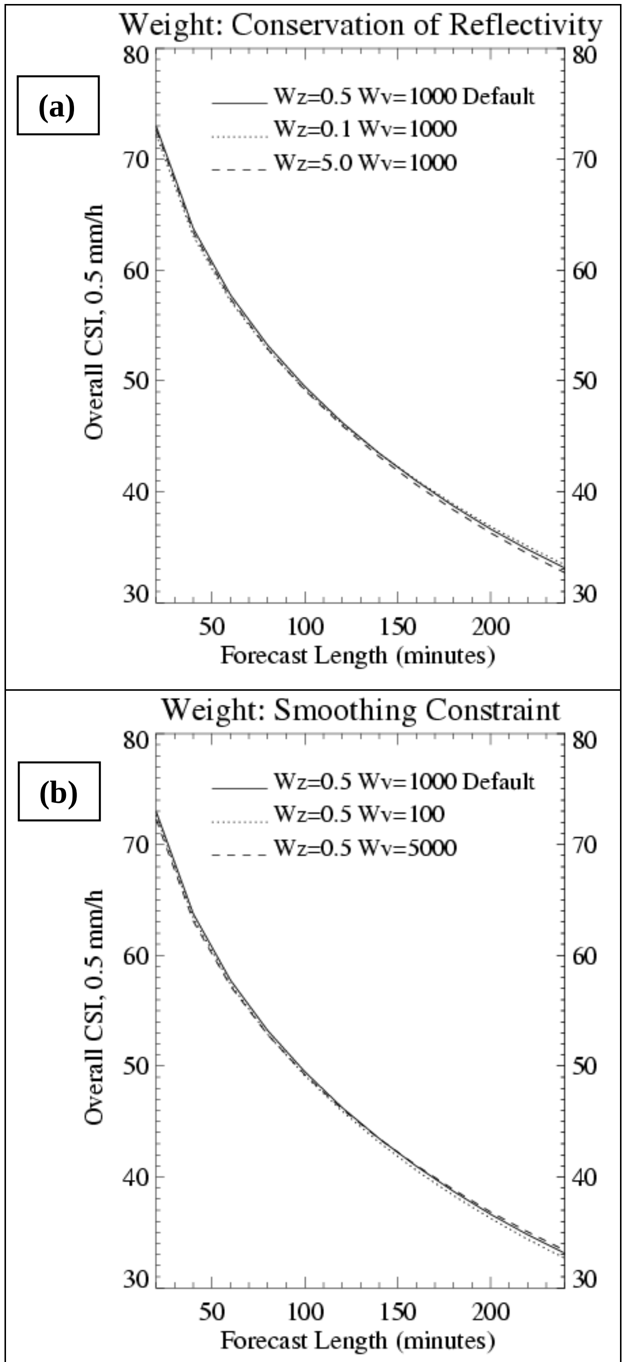

***Fig. 8**: Variation of the overall CSI for 0.5 mm/h as a function of the weights applied to a) the constraint for the conservation of reflectivity and b) the smoothness constraint on the velocity vectors.*

We had assumed that when using 3 input maps in our VET procedure, the obvious choice would be a time interval of 20 minutes, rather than of 10 minutes, so as to avoid the generation of forecasts from a velocity field representing short-lived accelerations or decelerations that are not expected to persist over longer forecasting periods. The results of Fig. 9

confirms our choice because the 10-minute interval provides a very marginal improvement only for forecasts less than one hour but would result into a larger deterioration in the quality of the longer term forecasts (> 2 h). However, the rather substantial loss in skill with 3 maps 10 minutes apart, for a total interval of 20 minutes prior T_0, is somewhat surprising compared with the results obtained with 2 maps 20 minutes apart which, as seen in then 2nd curve of Fig. 6, yielded nearly identical results to those of the default procedure. We suspect that quantization effects may be responsible.

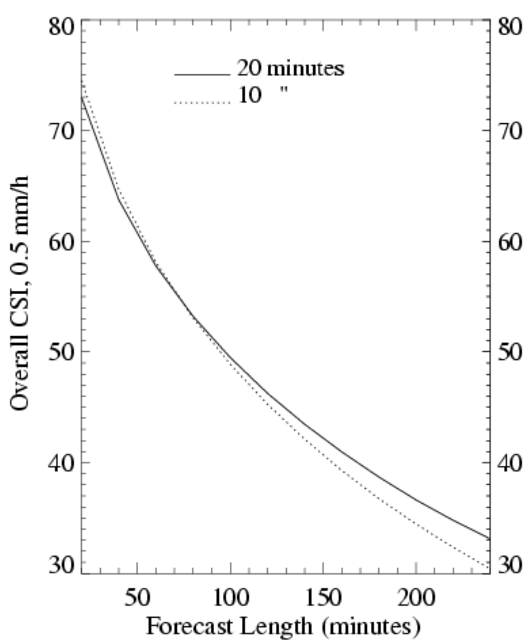

Fig. 9: *Variation of the overall CSI for 0.5 mm/h as a function of the time interval between the 3 maps used as input to the VET procedure.*

6- CONCLUSIONS

We have verified the skill of the MAPLE nowcasting scheme on a 4-month data set from the South Korean radar composite. CSI scores for 7 rainfall rates of 0.1, 0.2, 0.5, 1, 2, 5 and 10 mm/h have been computed for forecasts ranging from 20 minutes to 4 hours using the default VET input parameters, resulting into overall CSI scores of 58, 46, 39 and of 30% for 1-, 2-, 3- and 4-h forecasts respectively. Skill scores have also been presented as a function of radar range and the amount of smoothing.

Sensitivity tests have also been performed to determine the change in the quality of the forecasts using other plausible combinations of the VET input parameters. They have revealed that our initial choice of default input values essentially represents the optimum combination, although different vector densities and time interval between maps may slightly benefit (or worsen) shorter or longer term forecasts as seen for example in Figs 5 and 9. In other instances, the results from the entire sample remained essentially unchanged, although a more detailed analysis of individual events would be required to identify situations which may benefit from a particular combination of VET inputs.

The relatively small sensitivity to significant variations of the VET default parameters is a direct consequence of the fact that the major source of the loss in forecast skill cannot be attributed to errors in the forecast motion, but to the unpredictable nature of the storm growth and decay. The analysis using data from the real-time experiment presented in Part 2 further substantiates` this assertion.

7- ACKNOWLEDGEMENTS

This research was directly supported by a contract with the National Institute of Meteorological Research of South Korea, Contract # NIMR-2009-C-1.

8- REFERENCES

Germann, U., and I. Zawadzki, 2002: Scale-dependence of the predictability of precipitation from continental radar images. Part I: Description of the methodology. *Mon. Wea. Rev*., **130**, 2859-2873.

Germann, U., and I. Zawadzki, 2004: Scale-dependence of the predictability of precipitation from continental radar images. Part II: Probability forecasts. *J. Appl. Meteor*., **43**, 74-89.

Germann, U., I. Zawadzki, and B. Turner, 2006: Predictability of precipitation from continental radar images. Part IV: Limits to prediction. *J. Atmos. Sci*., **63**, 2092-2108.

Laroche, S., and I. Zawadzki, 1995: Retrievals of horizontal winds from single-Doppler clear-air data by methods of cross-correlation and variational analysis. *J. Atmos. Oceanic Technol*., **12**, 721-738.

Navon, I. M., and D. M. Legler, 1987: Conjugate-gradient method for large-scale minimization in meteorology. *Mon. Wea. Rev*., **115**, 1479-1502.

Seed, A. W., 2003: A dynamic and spatial scaling approach to advection forecasting. *J. Appl. Meteor*., **42**, 381-388

Turner, B. J., I. Zawadzki, and U. Germann, 2004: Predictability of precipitation from continental radar images. Part III: Operational nowcasting implementation (MAPLE). *J. Appl, Meteor*., **43**, 231-248